

Oxygen-Enhanced High Temperature Laminar Coflow Flames

Zhongxian Cheng^{*} and Robert W. Pitz[†]
Mechanical Engineering, Vanderbilt University, Nashville, TN, 37235

and

Beth Anne V. Bennett[‡] and Mitchell D. Smooke[§]
Mechanical Engineering, Yale University, New Haven, CT 06511

Three axisymmetric coflow laminar diffusion flames are investigated by laser-based diagnostics and detailed numerical simulation. Flame A is the base flame, with regular air as the oxidizer stream and 65% CH₄-35% N₂ as the fuel stream. Flame B and C are oxygen-enhanced coflow flames. Flame B has 100% O₂ as the oxidizer steam and 65% CH₄-35% N₂ as the fuel stream. Flame C has 100% O₂ as the oxidizer stream and 20% CH₄-80% N₂ as the fuel stream. Major species concentrations and temperature are measured by the Raman scattering technique as a function of axial and radial positions. The measured points have 0.28mm spatial resolution and $\pm 5\%$ uncertainty for flames A and B. A polarization separation technique is used to reduce laser-induced interference from the C₂ swan band and PAH. Computationally, a detailed kinetic mechanism (GRI-Mech 2.11 with nitrogen chemistry included) and a multi-component transport model are used to simulate the axisymmetric two-dimensional flame structure. Pure oxygen as the oxidizer causes intensive chemical reaction and makes flames B (~2400 K) and C (~2900 K) much shorter, stronger, and brighter than flame A. Because flames B and C are attached to the burner surface, a functional fit of experimental temperature data is used as a boundary condition. With uncertainty taken into account, model-data comparisons for major species concentration and temperature are very good for flames A and B. The general trend is predicted for flame C. Computational flame length and liftoff match the measured results very well. Computational results indicate the thermal NO dominates NO formation for flames B and C, while prompt NO dominates for flame A. The total radiative heat flux is measured along the axial direction at 25mm from the centerline of the burner for a series of oxygen-enhanced flames where O₂ concentration varies from 21% (volume fraction) to 100%. As expected, the radiative heat flux increases with oxidizer concentration.

I. Introduction

Liquid oxygen fuel flames are extensively used in rocket propulsion, and much relevant research has been done for the high pressure situation. At atmosphere pressure, oxygen-enriched flames have been used in industries such as glass and steel manufacturing to achieve high thermal efficiency. The fundamental effects of oxygen enrichment on flame characteristics are a reduction in flame length and an increase in flashback, blow off velocity gradient, and flammability range.^{1,2} The influence of oxygen enrichment on flame characteristics and on NO_x emissions has been studied. NO_x emissions can worsen because of the increased formation of thermal NO_x in the intensified combustion of the oxygen-enriched situation. However, oxygen-enhanced combustion can also result in conditions of stable combustion with reduced NO_x emissions. The addition of extra O₂ in the oxidizer noticeably

^{*} Graduate Student, Box 1592, Station B, Vanderbilt University, AIAA Student Member

[†] Professor, Box 1592, Station B, Vanderbilt University, AIAA Associate Fellow

[‡] Associate Research Scientist and Lecturer, Mechanical Engineering, Yale University

[§] Professor, Mechanical Engineering, Yale University, AIAA Associate Fellow

extends the lean flammability limits, and thus stable combustion can be achieved at leaner conditions, which are also characterized by reduced fuel consumption, lower flame temperatures and reduced NO_x emissions.³ NO formation during oxy/fuel combustion was studied with a counterflow burner^{4,5} and pathway and sensitivity analyses identified key reactions that contribute to the production of NO in oxy/fuel combustion where thermal NO was found to dominate.⁶

Coflow flame structures are closer to the practical flame configuration used in industry, and relevant experimental measurements with thermocouple, GC/MS, or optical diagnostics, along with numerical simulations, have been reported in Refs. 7-9. However, at the high temperatures occurring in oxygen-enhanced flames, thermocouples easily melt, and intrusive measurement becomes infeasible. Thus far, no non-intrusive measurements of detailed oxy/fuel coflow flame structure have been reported to the authors' knowledge. As the flame temperature goes up to 3000 K, strong emissions and interference adversely affect the measurement. At the same time, the fundamental combustion processes of oxygen/hydrocarbon fuel at low pressure need to be emphasized. In particular, validation of hydrocarbon mechanisms at high temperature is very important.

In this work, non-intrusive laser diagnostics have been applied to study the oxygen-enhanced coflow methane/air flame structure in detail. In addition, numerical modeling with detailed chemical kinetics and multi-component transport is performed for this two-dimensional flame structure. In this work, we study how oxygen-enriched concentration affects the coflow flame structure and other flame characteristics. Comparison of the data to modeling will help validate the chemical kinetics and molecular transport in the high temperature range (~3000 K).

II. Experimental Techniques

Measurement of major species concentration and temperatures is obtained by laser-based techniques using a laser diagnostic system similar to that described in Ref. 10. The oxy/fuel coflow burner is designed and built at Vanderbilt University for oxy/fuel flames (Fig. 1), and it has similar dimensions to the one used in Ref. 8. It consists of two concentric jets. The central fuel jet has normal diameter 4 mm, and the coflow oxidizer jet has a honeycomb (50 mm OD, 0.8 mm cell size) placed at the exit of the jet. Because the cell size is not very small compared to fuel jet diameter (3.9 mm ID), the top honeycomb is cut with EDM to allow the fuel tube to pass through, thus ensuring that the honeycomb will not disturb the fuel jet. The velocity profile for the fuel jet is parabolic and for the coflowing oxidizer should be flat. The gas flow rate is low enough to ensure that the flow is laminar. A carefully designed safety system (Fig. 2) is used for the high temperature oxygen-enriched flame experiment. It consists of a control box, solenoid valves, check valves, and a high pressure purge nitrogen line. Any flashback is unacceptable and prevented by the system. If an undesirable situation occurs, the fuel is purged from the burner by high-pressure nitrogen gas. All gas lines are cleaned oil-free for oxygen service. The burner is put on a precise translation stage (within 0.01 mm), which can move the burner in three directions. Each measurement is made along the axial direction of the burner. When the laser beam passes through the flame zone, the sample volume length is about 4.7mm, which is split into 25 individually measured points. The spatial resolution of point measurement is 0.28 mm. In order to map the entire flame structure, the measurement is performed at different axial locations (z direction) and radial locations (r direction).

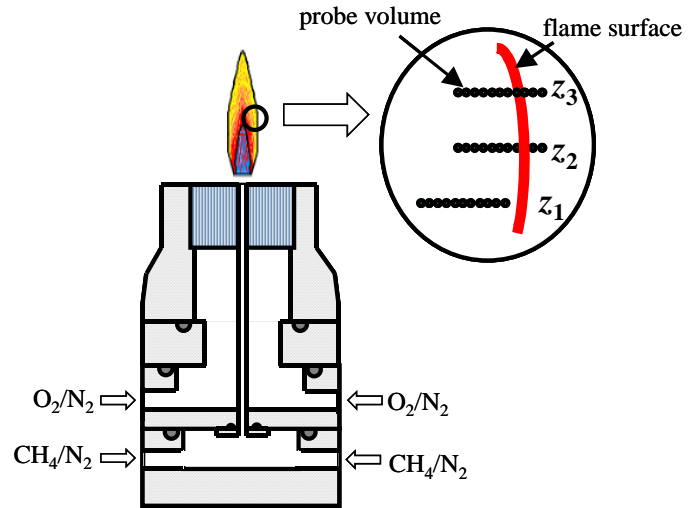


Figure 1. Schematic of oxy/fuel coflow burner

Table 1. Flame Parameters for Experiments and Computations

Flame	Jet	r (cm)	Composition	Velocity (cm/s)
A	Fuel	0.2	65% CH_4 / 35% N_2	$V_{\max}=76.0$
	Oxidizer	2.5	21% O_2 / 79% N_2	$V_{\text{avg}}=35.6$
B	Fuel	0.2	20% CH_4 / 80% N_2	$V_{\max}=144.8$
	Oxidizer	2.5	100% O_2	$V_{\text{avg}}=50.1$
C	Fuel	0.2	65% CH_4 / 35% N_2	$V_{\max}=140.9$
	Oxidizer	2.5	100% O_2	$V_{\text{avg}}=50.1$

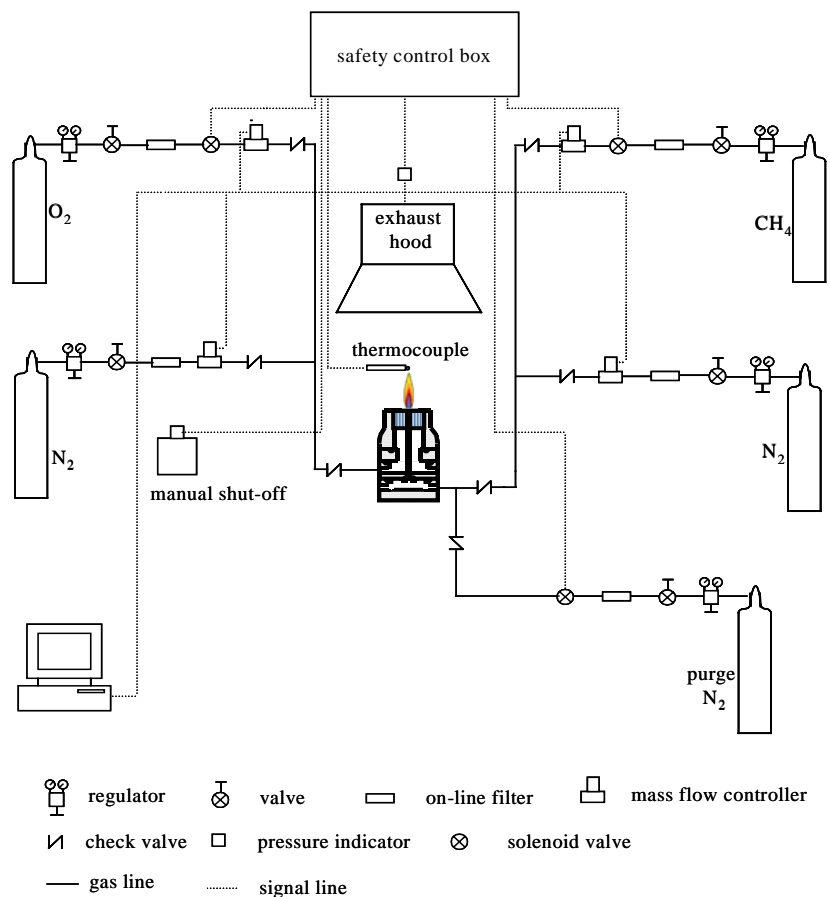


Figure 2. Schematic of the experimental safety system.

Three flames are examined by experiment and modeling. The flame parameters are given in Table 1. Flame A has regular air as the coflow oxidizer and 65% CH₄-35% N₂ as the fuel stream (photos are shown later in the paper). The average exit velocity of gases is 35 cm/s and leads to lifted steady laminar flame. Flame B has 100% O₂ as the oxidizer and 20% CH₄-80% N₂ as the fuel stream; the average exit velocity of 50 cm/s is not high enough to detach the flame from the burner surface. Flame C has 100% O₂ as the oxidizer and 65% CH₄-35% N₂ as the fuel stream; the average exit velocity of 50 cm/s is only 1/6 of the velocity necessary to lift the flame from the burner surface. In all cases, the fuel jet has $Re_{max} < 300$, so the flow is indeed laminar.

Non-premixed hydrocarbon flames have strong interferences that limit the accuracy of the Raman scattering technique. These interferences include various laser-induced fluorescence interferences from PAH and C₂. Also, laser induced incandescence

(LII) from soot and strong luminosity can contaminate the weak Raman signals. In order to reduce the various interferences, the fuel (methane) is diluted by nitrogen to 65% or 20%. Even with this dilution, PAH and C₂ fluorescence interference still exists. In order to reduce the interference further, visible Raman scattering with 532 nm excitation is used instead of UV Raman.¹¹ In this way, broadband interference is significantly decreased. In addition, polarization separated measurements¹¹⁻¹³ of the Raman and interference spectra are used to reduce the interference further. Two separate sets of data are taken for each measured point: one spectrum with the laser

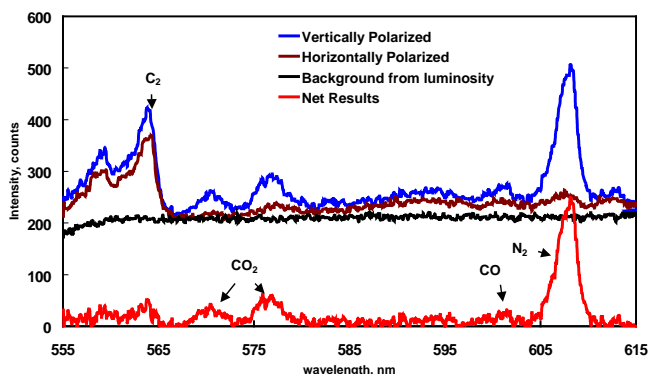


Figure 3. Example of polarization-separated spectra obtained in flame A at $z=28.5$ mm.

polarization vertical and one spectrum with the laser polarization horizontal. One spectrum contains the Raman signal plus broadband interference, while the other spectrum only contains broadband interference. This is because the Raman scattered light retains the polarization of the laser beam (vertical polarization), but the interference fluorescence is unpolarized. Therefore, the net Raman signal can be separated efficiently. One example is shown in Fig. 3. Even this approach doesn't eliminate C₂ Swan band fluorescence completely. C₂ fluorescence has a well-characterized spectrum and exists at specific wavelengths. By properly selecting signal channel and background correction, the influence of C₂ can be reduced

significantly as well. Interferences from luminosity can be eliminated by taking the background measurement when the laser is not fired. All of these strategies work well for most regions inside flames, except in some regions of strongly oxygen-enhanced flames. In those regions, various interferences are so strong that the Raman signal cannot be made to yield reasonable experimental data.

III. Numerical Modeling

The main assumptions in the numerical model are as follows. The gas is considered to be a Newtonian fluid at steady state, the low Mach number assumption and the ideal gas law are invoked, and the Soret and Dufour effects are considered negligible. The chemical kinetics are modeled using GRI-Mech 2.11, including nitrogen chemistry, resulting in a mechanism that contains 50 species participating in 275 reversible reactions.¹⁴ All thermodynamic, chemical, and multicomponent transport properties are evaluated using the CHEMKIN¹⁵ and TPLIB¹⁶ subroutine libraries, which have been further optimized for increased speed.¹⁷ The numerical model includes an optically thin radiation submodel with three significant radiating species (H_2O , CO , and CO_2). No soot model is included.

The conservation equations of mass, momentum (2 components, since each flame is axisymmetric), energy, and individual species mass (for each of the 50 species) are rewritten using the vorticity-velocity formulation, in which the dependent variables are two velocity components, vorticity, temperature, and 50 species concentrations. The boundary conditions are similar to those employed in Ref. 9, with the following exceptions. At the bottom boundary (the burner surface), a temperature profile is applied; this profile is obtained by doing a functional fit of extrapolated experimental data for each flame. While the velocity profiles at the bottom boundary are parabolic in the inner tube and flat in the outer tube (as in Ref. 9), the maximum velocity in the inner tube is adjusted so that the mass flow rate matches experimental values, taking into consideration the applied temperature profile (and the accompanying reduction of density with increased temperature). Finally, at the outer radial boundary of the computational domain, free stream boundary conditions are applied (*i.e.*, radial derivatives of dependent variables vanish).

The numerical solution techniques used to solve the system of governing equations and boundary conditions are similar to those described in Ref. 9. Only a brief overview is given here. Because each flame is axisymmetric, the computational domain is two-dimensional. It extends several burner radii in the radial direction, and it also extends several flame lengths downstream in the axial direction. This domain is then spanned by a grid of 15,000 to 25,000 adaptively chosen grid points, and the 54 strongly coupled, highly nonlinear equations are discretized and solved at all points simultaneously using the LRR (local rectangular refinement) solution-adaptive gridding method, which incorporates a damped, modified Newton solver. For each of the flames, the grid adapts based on gradients of computed temperature and OH, and the adaptation/solution process continues until a termination criterion is met.

IV. Results and Discussion

A. Computed Contours of Temperatures and Species for Flames A, B, and C

Before comparing experimental and computational data, we examine some of the computational results in order to observe the general features of flames A, B, and C. Figures 4, 5, and 6 display contours of temperatures and some selected species, in a portion of the computational domain, for flames A, B, and C, respectively. In Figure 4, it can be seen that the hottest part of flame A (the base case) occurs in a wishbone-shaped region, and that flame A is indeed lifted from the burner surface. The maximum temperature in flame A is 1947 K. The fuel (methane) is consumed within a short distance of the burner surface, and the methane and oxygen mostly do not spatially coincide, except for some small amounts of oxygen that “leak” inside the non-premixed flame front. The maximum oxygen concentration is 21%, occurring

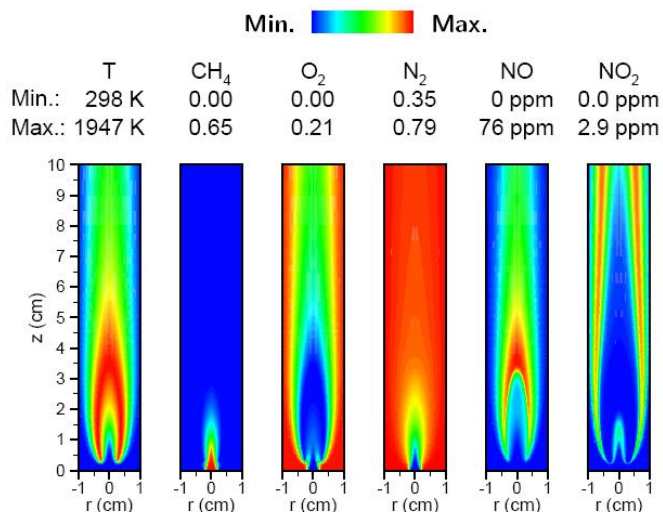


Figure 4. Computed isotherms and contours of selected species concentrations in flame A.

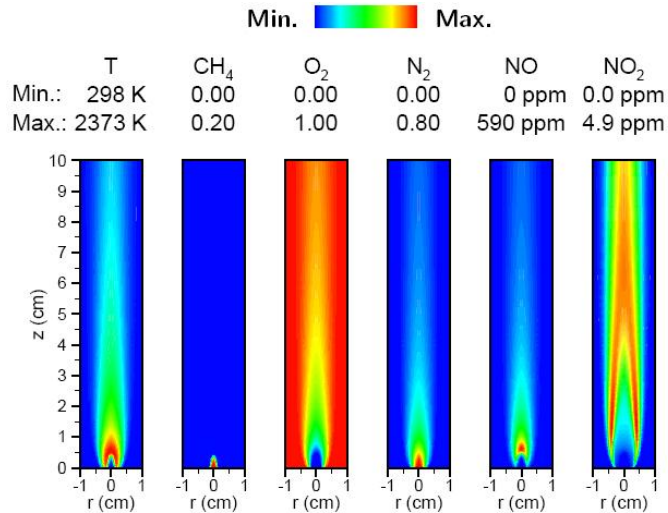


Figure 5. Computed isotherms and contours of selected species concentrations in flame B.

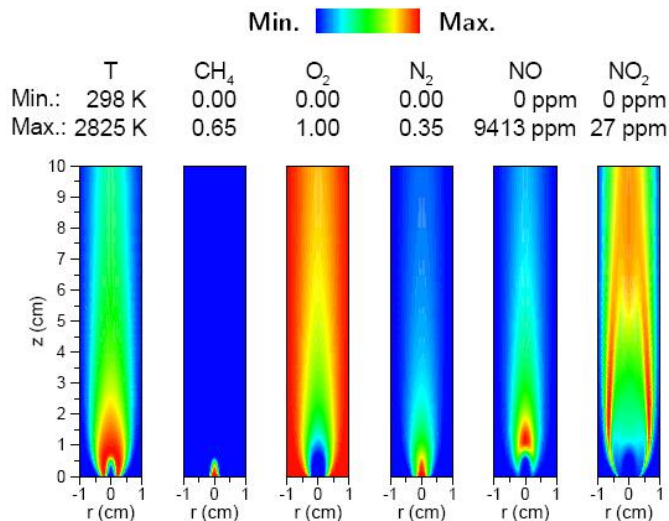


Figure 6. Computed isotherms and contours of selected species concentrations in flame C.

statements similar to those made for flame B can again be made for flame C. Because flame C's oxidizer is pure oxygen and because its fuel is not as heavily nitrogen-diluted as in flame B, the maximum nitrogen concentration is 35%, which might lead one to expect a reduction in NO and NO₂ concentrations. However, the opposite is true: peak NO concentrations in flame C are about 16 times larger than in flame B, and about 120 times larger than in flame A.

The various peak amounts of NO in the three flames can be explained as follows. It is known that NO formation in flames occurs via four routes: the Zeldovich (or "thermal") route, which is important at temperatures exceeding approximately 1850 K; the N₂O decomposition route, which is more important at high pressures; the NNH route, which produces NO in very small quantities; and the prompt route, which is dominant at temperatures under 1850 K. For more information and some discussion on these various routes, see Refs. 18 and 19. To determine which routes are largely responsible for the NO formation in flames A, B, and C, additional calculations have been performed in which the various NO formation routes are systematically retained in or removed from in the chemical mechanism; a similar method has been used in Ref. 18. Results of these additional calculations show that 85% of the peak NO in flame A comes from the prompt route, which is not surprising since the maximum temperature in flame A is rather low. In flame B, 92% of the peak NO is thermal NO, as expected given that the flame's peak temperature is considerably above 1850 K. Also, the residence time of a fluid particle on the centerline of the flame within the

in the oxidizer stream. Nitrogen concentrations range from 35% (in the fuel stream) to 79% (in the oxidizer stream); no portion of the flame is nitrogen-free. Comparison of pollutants NO and NO₂ shows that NO₂ occurs in much smaller quantities than NO, so a strategy for reducing emissions should target NO concentrations. The maximum NO concentrations of 76 ppm occur just downstream of the hottest region in the flame. NO concentrations are addressed in greater detail at the end of this subsection.

In Figure 5, the most striking features of flame B are that it is shorter (flame length is discussed in a later section in more detail) and hotter than flame A (peak temperature has increased by over 400 K, to 2373 K). Also, flame B is attached to the burner surface. The hottest portion of the flame again occurs in a wishbone-shaped region. The fuel is consumed over a much smaller axial distance than in flame A, and the maximum CH₄ concentration is now 20%. Oxygen concentrations range from 0% to 100%, and there is very little, if any, leakage of O₂ across the non-premixed flame front. Because there is no nitrogen in the oxidizer stream, the minimum N₂ concentration is 0%. Comparison of pollutants NO and NO₂ again shows that the concentrations of NO dominate those of NO₂. More importantly, however, is the fact that the peak NO concentration in flame B is significantly higher than in flame A; it has increased by almost an order of magnitude. This increase is discussed further at the end of this subsection.

From Figure 6, it is apparent that the hottest of the three flames is flame C, whose peak temperature is 2825 K. This flame is intermediate in length between flames A and B, and it is attached to the burner, like flame B. The high temperature region is again wishbone-shaped. Regarding the methane and oxygen profiles,

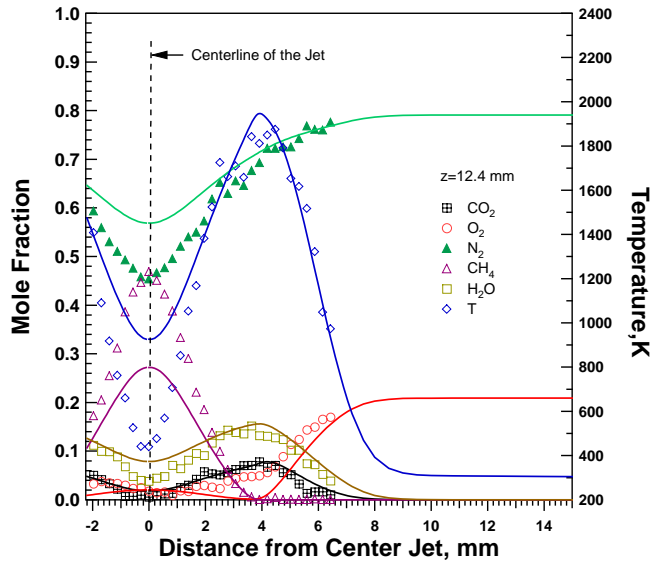


Figure 7. Experimental and computed species and temperature profiles for flame A at $z/d=3.1$.

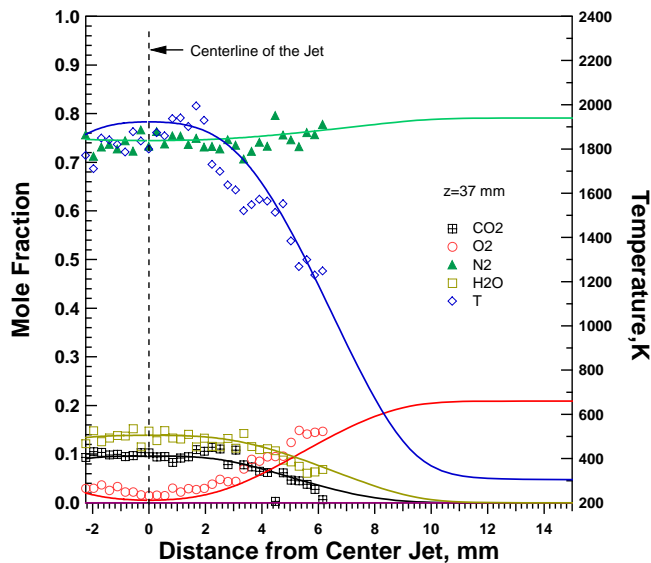


Figure 8. Experimental and numerical-predicted species and temperature profiles for flame A at $z/d=9.3$.

is the strongest factor; a different mechanism can produce a computed liftoff that is twice as large as with GRI-Mech 2.11. Since GRI-Mech 2.11 has a high extinction strain rate, the flame is able to survive very close to the burner surface (where strain rates are largest), leading to a relatively small liftoff. In Fig. 7, the major products (H_2O , CO_2) show very good agreement between experimental data and predictions. The flame front is located at a radial position of 4 mm and the peak temperature is about 1950 K. The major species concentrations and temperature profiles in the radial direction at $z=37$ mm are given in Fig. 8. Temperature, H_2O , and CO_2 profiles all show a plateau near the centerline and decay outside of the flame zone. Measured CO_2 and H_2O match the predicted results very well at most of the radial locations, while the measured temperature data show some noise since this axial location is close to the soot region (yellow colored zone).

Flame B is an oxygen-enhanced flame with pure oxygen as the oxidizer. In order to make the Raman scattering measurement with less interference, the fuel (CH_4) is diluted by N_2 to a 20% CH_4 -80% N_2 mixture. Because oxygen is used instead of air, the flame temperature is increased significantly with N_2 elimination, and the flame becomes a tiny blue flame at this fuel concentration. Since the laminar flame speed is 10 times increased for the methane

region exceeding 1850 K is about 5.2 ms. Finally, in flame C, 97% of the peak NO is attributable to thermal NO, which is again expected since the peak temperature is so high. However, a major factor contributing to the very large amounts of NO in flame C is the fact that the residence time on the centerline in the 1850 K (or higher) region is 14.2 ms - approximately 3 times that in flame B.

B. Data-Model Comparisons of Temperature and Species Profiles for Flame A, B, and C

The major species concentrations are measured as a function of the two coordinate directions (axial z and radial r) with the Raman scattering technique. The radial profiles are measured at axial positions starting near the burner surface ($z=0.4$ mm) in 2 mm or 4 mm increments. The measured points range from one side of centerline (-2.24 mm) to other side of the centerline (60 mm) in the radial direction and have 0.28 mm spatial resolution.

For comparison purposes, the base flame A is measured first. A similar flame was studied by experiment and simulation in Ref. 7. Radial profile measurements are made for flame A at 11 axial locations (from $z/d \approx 0$ to $z/d \approx 10$, d is the radius of fuel jet). The measurements from two selected positions at $z/d=3$ and $z/d=9$ are shown in Figs. 7-8. Modeling results are shown on the same plot. Flame A is a lifted flame, and the flame base in the laboratory is observed to be about 6 mm above burner surface. In Fig. 7 ($z=12.4$ mm), CH_4 is not consumed yet and the measured concentration is 0.45 (mole fraction) near centerline while computed CH_4 concentration is about 0.29 (mole fraction). The predicted liftoff flame location (2.7 mm) is lower than observed (6 mm above burner surface). The difference between measured and computed liftoff may be caused by heat loss treatment or the choice of boundary conditions since the computed flame height is very sensitive to these factors.⁹ However, for this flame, the choice of chemical mechanism

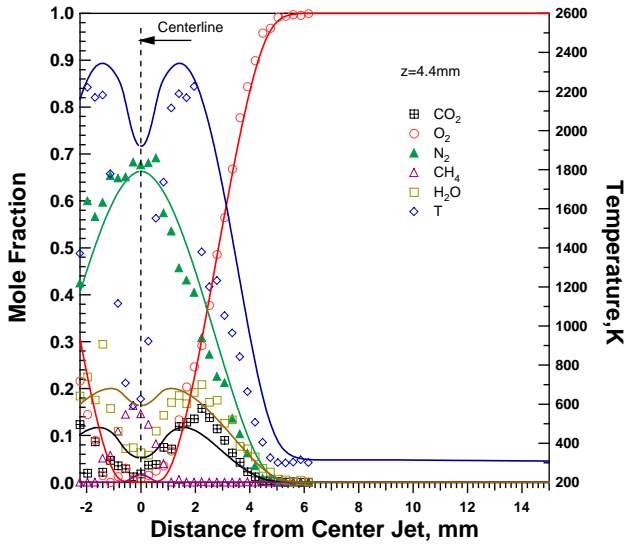


Figure 9. Experimental and numerical-predicted species and temperature profiles for flame B at $z/d = 1$.

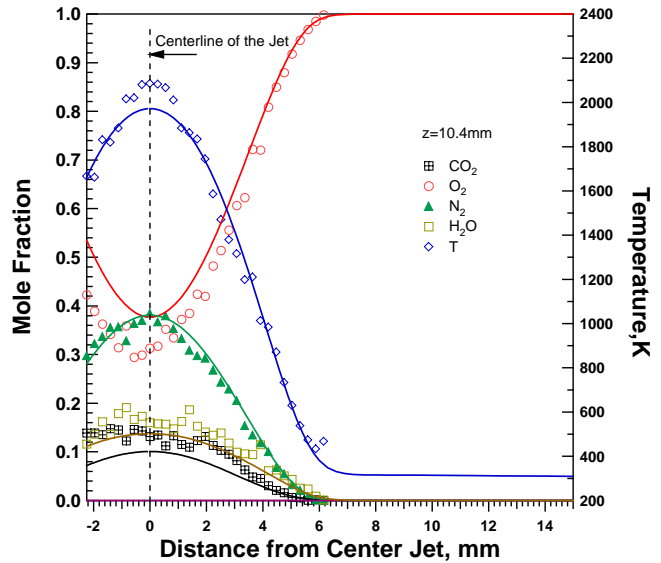


Figure 10. Experimental and numerical-predicted species and temperature profiles for flame B at $z/d = 2.6$.

between pure oxygen and air,²⁰ flame B is attached to the burner surface. This makes it more difficult to obtain appropriate boundary conditions (initial temperature and reactant concentration) for modeling. Fits of extrapolated temperature data are used for the modeling, as described in Section III. A comparison of major species and temperature profiles at axial location $z=4.4\text{mm}$ is given in Fig. 9. In the inner layer (near the centerline), the measured temperature, CO_2 , and H_2O are lower than predicted results. In the outer layer ($r > 2\text{ mm}$), the O_2 and H_2O profiles show good agreement for model-data comparison, but the measured temperature is slightly lower than the prediction. The general trend in the CO_2 profiles are similar between experiment and simulation. The comparisons for the same flame at $z=10.4\text{ mm}$ are given in Fig. 10. General agreement is obtained for the CO_2 , H_2O , N_2 , and temperature profiles, particularly when $r > 2\text{ mm}$.

Flame C is another oxygen-enhanced flame with pure oxygen as the oxidizer. Among the three flames examined here, flame C has the highest flame temperature ($\sim 2900\text{ K}$) and presents the most challenges for the experimental technique. Raman signals are very weak compared to the strong emissions from the intensive combustion of the

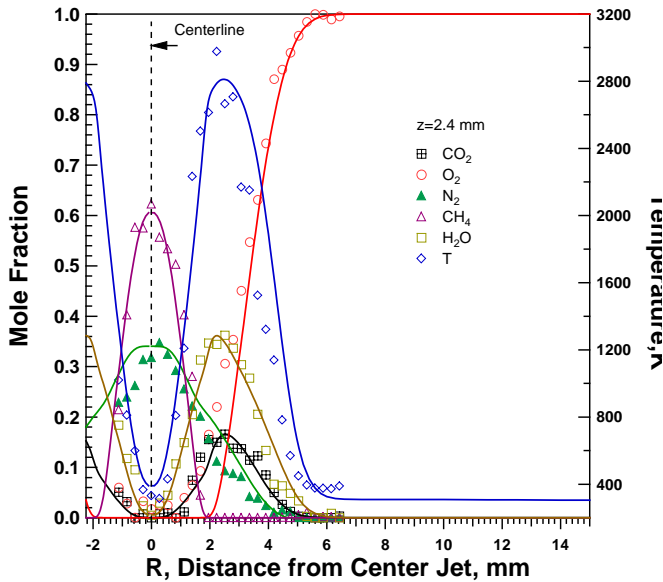


Figure 11. Experimental and numerical-predicted species and temperature profiles for flame C at $z/d = 0.6$.

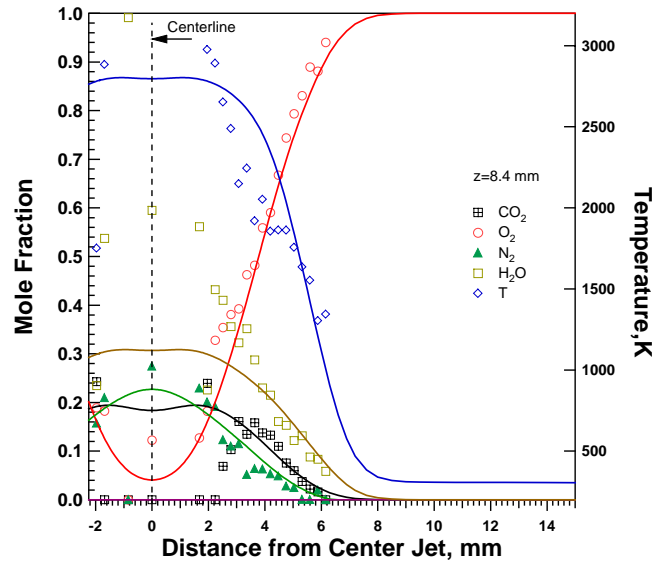


Figure 12. Experimental and numerical-predicted species and temperature profiles for flame C at $z/d = 2.1$.

pure oxygen flame. Therefore, the flame formed by pure fuel (100% CH₄) with pure oxygen (100% O₂) made the Raman scattering measurement infeasible. The fuel (CH₄) has to be diluted to a 65% CH₄-35%N₂ mixture. The flame is attached to the burner surface. Compared to flame B, the fuel (CH₄) concentration increases from 20% (mole fraction) to 65% and peak temperatures increases to ~2900 K. Selected species and temperature profiles in the radial direction are given in Fig. 11 and Fig. 12. Figure 11 shows that, at z=2.4 mm, the fuel is not consumed yet, and the profiles for CH₄, H₂O, O₂, and N₂ show a very good agreement for data-model comparisons. The peak temperature exceeds 2800 K at this axial location and is much higher than in flames A and B. At z=8.4 mm (Fig. 12), useful experimental data are only available when $r > 3$ mm because of strong interference from flame emissions.

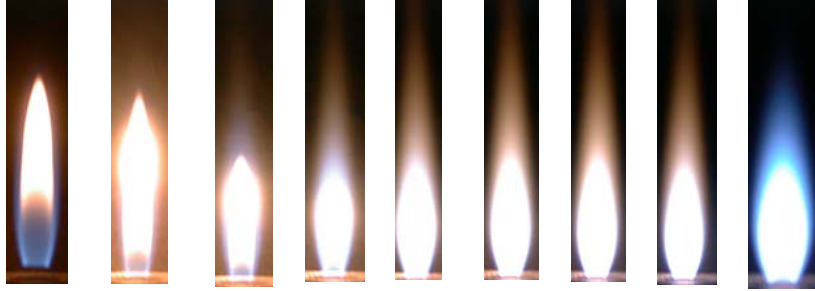


Figure 13. Photographs taken for the oxygen-enhanced flames to show relative length (from left to right, oxygen concentration varies from 21%, 30%, 40%, 50%, 60%, 70%, 80%, 90% to 100%, fuel (CH₄) concentration is constant. Average gas velocity for both jets are 50 cm/s except for 21% case whose average gas velocity for both jets are 35 cm/s.

The model-data comparison ($r > 3$ mm) shows good agreement in outer layer of the flame.

C. Flame Length and Liftoff

Oxygen enhancement significantly affects flame length. For a given fuel concentration, the higher the oxygen concentration is, the shorter the flame is. This can be found from visible flame length measurement. The visual appearances (direct photograph with the exact same focus setting) of the oxygen-enhanced flame are shown in the Fig. 13. From left to right, oxygen concentration varies from 21% (mole fraction) to 30%, and then up to 100% in 10% increments. The average gas velocity is 35 cm/s for the 21% case and 50 cm/s for all other cases. It is found that the flame color changes from blue to bright, the flame length changes from long to shorter, and the flame radial dimension from narrow to wider, with increasing oxygen concentration. The length of jet diffusion flames has been studied in Refs. 21 and 22 by analytical methods and by experimental verification, and it is defined as the z at which the centerline local equivalence ratio is unity (stoichiometric ratio). It is sometimes referred as the mixture-strength flame length H_f .²³ In contrast to H_f , the maximum temperature flame length H_T ²⁴ is defined as the z at which the temperature along the centerline reaches the maximum. It is argued that H_T is a good surrogate to H_f ,²⁴ and it will be used in this work.

From the analytical expression derived by Roper,²¹ the flame temperature T_f and mass diffusivity (D_0) affect flame length. For given mixture, D_0 is a constant, so flame temperature (T_f) should be the main factor to affect the flame length. Because of the limited temperature data available along the centerline in this work, the measured maximum flame temperature along the centerline is obtained by extrapolation. The computational/experimental comparison for flame length is given in Table 2 for flames A, B, and C. From Table 2, very good agreement exists within the experimental uncertainty for computed flame length and measured flame length. Here, the flame liftoff is defined as the lowest z location at which temperature is greater than 1000 K. Comparisons of liftoff are also listed in Table 2. As observed in the laboratory, flame A is lifted and flames B and C are attached to the burner surface. The measured liftoff for flame A is given by a range (0.44 cm~0.84 cm), because no measured data is available between axial locations 0.44 cm and 0.84 cm.

Table 2. Flame Length and Liftoff comparisons for Three Flames

Flame	Method	H_T (cm)	Liftoff (cm)	T_{max} at centerline (K)
A	Computational	3.50	0.27	1928
	Experimental	3.24±0.2	0.44~0.84	2014±100
B	Computational	0.58	0	2373
	Experimental	0.64±0.1	0	2400±120
C	Computational	0.86	0	2797
	Experimental	0.84±0.1	0	2850±150

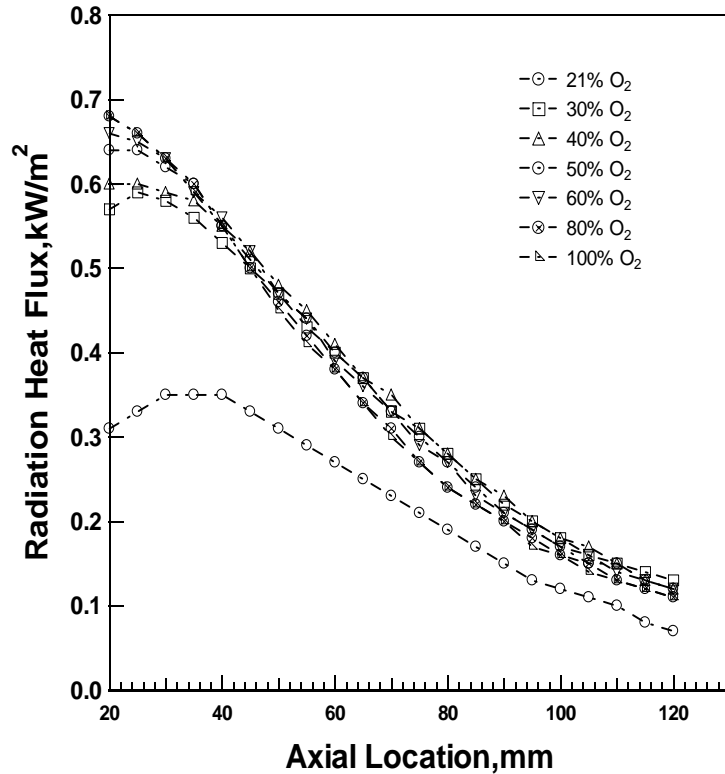


Figure 14. Total radiation flux distribution parallel to the flame axis at a distance of 25mm for various oxygen-enhanced flames.

The radiative flux for 21% O_2 case reaches a maximum at 40mm near flame height H_T , where the flame temperature peaks along the centerline. For highly oxygen-enhanced cases (90% O_2 ~100% O_2), the maximum radiative flux occurs at axial location 20 mm, because of the shorter flame lengths. Obviously, the total radiative heat flux increases dramatically when the oxygen concentration is increased, because of the increase in flame temperature. These high radiative flux characteristics lead to the wide application of oxygen-enhanced flames in industry.

V. Conclusion

Three axisymmetric coflow laminar diffusion flames are investigated by laser-based diagnostics and detailed numerical simulation. Flame A is the base flame that has regular air as the oxidizer. Flames B and C are oxygen-enhanced flames with pure oxygen as the oxidizer.

Major species concentrations and temperature are measured by a Raman scattering technique, as the function of axial and radial positions. The measured points have 0.28 mm spatial resolution and $\pm 5\%$ uncertainty for flames A and B. A polarization separation technique is used to reduce laser-induced interference from the C_2 Swan band and PAH. Computationally, a detailed kinetic mechanism (GRI-Mech 2.11 including nitrogen chemistry) and a multicomponent transport model are used to simulate the axisymmetric two-dimensional flame structure.

Pure oxygen as the oxidizer causes intensive chemical reaction and makes flame B (~2400 K) and flame C (~2900 K) much shorter, stronger, and brighter than flame A. Because flames B and C are attached to the burner surface, it is necessary to use an extrapolated functional fit of measured temperatures as the boundary condition. Taking uncertainty into consideration, model-data comparisons for major species concentrations and temperature give very good agreement for flames A and B. The general trend is predicted for flame C. Computational flame length and liftoff match the measured results very well. Computational results indicate thermal NO dominating NO formation for flames B and C, while prompt NO dominates for flame A. The total radiative heat flux is measured along the axial direction at a 25 mm distance from the centerline of the burner for a series of oxygen-enhanced flames where O_2 concentration varies from 21% (volume fraction) to 100%. As expected, the total radiative heat flux increases with oxidizer concentration.

D. Heat and Radiative Flux Measurement

Oxygen-enhanced flames obviously have higher flame temperatures than fuel/air flames, and radiation is the dominant heat transfer mechanism inside an oxygen-enhanced flame. More than 90% of the energy is released by radiation,² while the role of convection diminishes.

Measurements of total radiative heat flux distribution are made along the height of the flames using a Medtherm Radiation Heat Flux Transducer (64P-02-22-BaF2W, 150° viewing angle). A similar transducer has been used to measure radiation in various jet diffusion flames.²⁵⁻²⁷ In this work, the transducer traverses the flame parallel to the z axis, facing the axis at a radial distance of 25 mm. This location corresponds closely with the maximum radiant flux and has been found to be the appropriate location to estimate the radiant fraction from a single near-field heat-flux measurement²⁶ for flame A. The flame boundaries are entirely within the viewing angle of the sensor, except points far from the exit where contributions to radiative heat flux are small. Measurements of total radiative heat flux are given in Fig. 14.

Acknowledgments

This research work is partially supported by the Gas Research Institute, and Air Products provided most of the gases for the oxygen-enhanced combustion experiment. The authors give special thanks for this support.

References

- ¹Pourkashanian, M., Yapp, L., and Williams, A., "The Use of Oxygen Enrichment in Combustion Technology," Paper presented at *Applied Energy Research Conference*, Swansea, September, 1989.
- ²Baukal, C. E., "Basic Principles," in *Oxygen-Enhanced Combustion*, ed. by Baukal, C. E., CRC Press, Boca Raton, 1998, pp. 2-42.
- ³Qin, W., Ren, J.-Y., Egolfopoulos, F.N., Wu, S., Zhang, H., and Tsotsis, T.T., "Oxygen Composition Modulation Effects on Flame Propagation and NO_x Formation in Methane-Air Premixed Flames," *Proceeding of the Combustion Institute*, Vol. 28, 2000, pp. 1825-1831.
- ⁴Naik, S.V. and Laurendeau, N., "Quantitative Laser-Saturated Fluorescence Measurements of Nitric Oxide in Counter-flow Diffusion Flames under Sooting Oxy-fuel Conditions," *Combustion and Flame*, Vol. 129, 2002, pp. 112-119.
- ⁵Naik, S.V., Laurendeau, N.M., Cooke, J.A., and Smooke, M.D., "Effect of Radiation on Nitric Oxide Concentration under Sooting Oxy-Fuel Conditions," *Combustion and Flame*, Vol. 134, 2003, pp. 425-431.
- ⁶Sung, C.J. and Law, C.K., "Dominant Chemistry and Physical Factors Affecting NO Formation and Control in Oxy-Fuel Burning," *Proceeding of the Combustion Institute*, Vol. 27, 1998, pp. 1411-1418.
- ⁷Smooke, M.D., Lin, P., Lam, J.K., and Long, M.B., "Computational and Experimental Study of a Laminar Axisymmetric Methane-Air Diffusion Flame," *Proceedings of the Combustion Institute*, Vol. 23, 1990, pp. 575-582.
- ⁸Smooke, M.D., McEnally, C.S., Pfefferle, L.D., Hall, R.J., and Colket, M.B., "Computational and Experimental Study of Soot Formation in a Coflow, Laminar Diffusion Flame," *Combustion and Flame*, Vol. 117, 1999, pp. 117-139.
- ⁹Bennett, B.A.V., McEnally, C.S., Pfefferle, L.D., and Smooke, M.D., "Computational and Experimental Study of Axisymmetric Coflow Partially Premixed Methane/Air Flames," *Combustion and Flame*, Vol. 123, 2000, pp. 522-546.
- ¹⁰Cheng, Z., Wehrmeyer, J.A., and Pitz, R.W., "Lean or Ultra Lean Stretched Planar Methane/Air Flames," *Proceedings of the Combustion Institute*, Vol. 30, 2004, in press.
- ¹¹Osborne, R.J., Wehrmeyer, J.A., and Pitz, R.W., "A Comparison of UV Raman and Visible Raman Techniques for Measuring Non-Sooting Partially Hydrocarbon Flames," *AIAA 2000-0776*, 2000, 38th Aerospace Science Meeting, Reno, NV.
- ¹²Grunefeld, G., Beushausen, V., and Andresen, P., "Interference Free UV Laser Induced Raman and Rayleigh Measurement in Hydrocarbon Combustion Using Polarization Properties," *Applied Physics B*, Vol. 61, 1995, pp. 473-478.
- ¹³Kanpp, M., Luczak, A., Beuhausen, V., Hentschel, W., Manz, P., and Andresen, P., "Polarization Separated Spatially resolved Single laser Shot Multispecies Analysis in the Combustion Chamber of a Realistic SI Engine with a Tunable KrF Excimer Laser," *Proceedings of the Combustion Institute*, Vol. 26, 1996, pp. 2589-2596.
- ¹⁴Bowman, C.T., Hanson, R.K., Davidson, D.F., Gardiner, Jr., W.C., Lissianski, V., Smith, G.P., Golden, D.M., Frenklach, M., Wang, H., and Goldenberg, M., 1995, <http://www.gri.org>.
- ¹⁵Kee, R.J., Warnatz, J., and Miller, J. A., "A Fortran Computer Code Package for the Evaluation of Gas-Phase Viscosities, Conductivities, and Diffusion Coefficients," Sandia National Laboratory Rept., 1983, SAND83-8209.
- ¹⁶Kee, R.J., Dixon-Lewis, G., Warnatz, J., Coltrin, M.E., and Miller, J.A., "A Fortran Computer Package for the Evaluation of Gas-Phase, Multicomponent Transport Properties," Sandia National Laboratory Rept., 1986, SAND86-8246.
- ¹⁷Giovangigli, V., and Darabiha, N., in *Mathematical Modeling in Combustion and Related Topics*, C.-M. Brauner and C. Schmidt-Laine, eds., Nijhoff, Dordrecht, 1988, pp. 491-503.
- ¹⁸Smooke, M.D., Ern, A., Tanoff, M.A., Valdati, B.A., Mohammed, R.K., Marran, D.F., and Long, M.B., "Computational and Experimental Study of NO in an Axisymmetric Laminar Diffusion Flame," *Proceedings of the Combustion Institute*, Vol. 26, 1996, pp. 2161-2170.
- ¹⁹Bozzelli, J.W., Chang, A.Y., and Dean, A.M., "Analysis of the Reactions H+N₂O and NH+NO: Pathways and Rate Constants Over a Wide Range of Temperature and Pressure," *Proceedings of the Combustion Institute*, Vol. 25, 1994, pp. 965-974.
- ²⁰Glassman, I., *Combustion*, 3rd Edition, Academic Press, San Diego, CA, 1996.
- ²¹Roper, F.G., "The Prediction of Laminar Jet Diffusion Flame Sizes: Part I. Theoretical Model", *Combustion and Flame*, Vol. 29, 1977, pp. 219-226.
- ²²Roper, F.G., Smith, C., and Cunningham, A.C., "The Prediction of Laminar Jet Diffusion Flame Sizes: Part II. Experimental Verification," *Combustion and Flame*, Vol. 29, 1977, pp. 227-234.
- ²³McEnally, C.S. and Pfefferle, L.D., *Proceedings of the Combustion Institute*, Vol. 27, 1998, pp. 1539-1547.
- ²⁴McEnally, C.S. and Pfefferle, L.D., "Experimental Study of Nonfuel Hydrocarbon Concentrations in Coflowing Partially Premixed Methane/Air Flames," *Combustion and Flame*, Vol. 118, 1999, pp. 619-632.
- ²⁵Jeng, S.-M. and Faeth, G.M., "Radiative Heat Fluxes Near Turbulent Buoyant Methane Diffusion Flame," *Journal of Heat Transfer*, Vol. 106, November 1984, pp. 886-888.
- ²⁶Sivathanu, Y.R. and Gore, J.P., "Total Radiative Heat Loss in Jet Flames from Single Point Radiative Flux Measurements," *Combustion and Flame*, Vol. 94, 1993, pp. 265-270.
- ²⁷Souil, J.M., Joulain, P., and Gengembre, E., "Experimental and Theoretical Study of Thermal Radiation from Turbulent Diffusion Flames to Vertical Target Surfaces," *Combustion Science and Technology*, Vol. 41, 1984, pp. 69-81.